Granular and fluid washboards

I. J. Hewitt[1]†, N. J. Balmforth[1] and J. N. McElwaine[2]

[1] Department of Mathematics, University of British Columbia, Vancouver, V6T 1Z2, Canada

[2] Department of Applied Mathematics and Theoretical Physics, University of Cambridge,
Cambridge CB3 0WA, UK

We investigate the dynamics of an object towed over the surface of an initially flat, deformable layer. Using a combination of simple laboratory experiments and a theoretical model, we demonstrate that an inclined plate, pivoted so as to move up and down, may be towed steadily over a substrate at low speed, but become unstable to vertical oscillations above a threshold speed. That threshold depends upon the weight of the plate and the physical properties of the substrate, but arises whether the substrate is a viscous fluid, a viscoplastic fluid, or a granular medium. For the latter two materials, the unstable oscillations imprint a permanent rippled pattern on the layer, suggesting that the phenomenon of the 'washboard road' can arise from the passage of a single vehicle (i.e. the absolute instability of a flat bed). We argue that the mechanism behind the instability originates from the mound of material that is pushed forward ahead of the object: the extent of the mound determines the resultant force, whereas its growth is controlled by the object's height relative to the undisturbed surface, allowing for an unstable coupling between the vertical motion and the substrate deformation.

---

1. Introduction

It is commonly believed that the washboard patterns that appear on gravel or sandy roads arise due to the repeated passage of vehicles, with a critical role played by a vehicle running over the wake imprinted on the granular bed by preceding vehicles. With this image in mind, and following on from earlier work by Mather (1963), a number of recent experiments have generated washboards in the laboratory by continually circulating wheels or ploughs around the surface of sandy layers (either by rotating the underlying table or moving the mounting holding the ploughing object around a circular track; Taberlet, Morris & McElwaine 2007; Bitbol *et al.* 2009; Percier *et al.* 2011). Discrete-element simulations also reproduce the phenomenon and show that compaction and segregation are not critical factors in washboard dynamics. Indeed, the primary controlling variables appear to be simply the paddle speed and weight, and the density of the granular substrate. Other models for the washboard phenomenon are presented by Mays & Faybishenko (2000) and Both, Hong & Kurtze (2001).

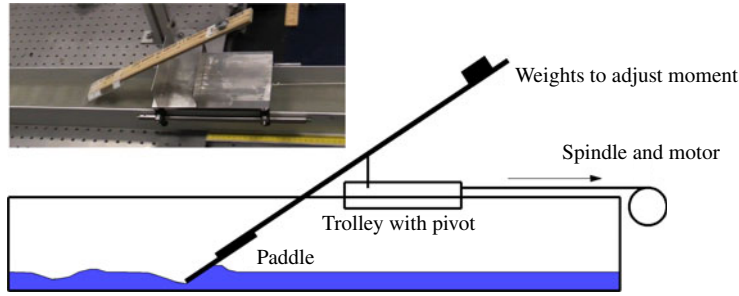† Email address for correspondence: hewitt@math.ubc.ca

FIGURE 1. (Colour online available at journals.cambridge.org/flm) Experimental setup. A motor pulls the trolley at fixed speed along a track above a channel (3 m long and 10 cm wide) filled with either glass beads or a fluid. A rectangular paddle (5 cm wide) is pivoted 23 cm from a vertical metal plate fitted on the trolley, making an angle of about $\alpha = 30°$ with the surface of the substrate. The effective weight of the paddle is adjusted by adding weights to the arm to alter the net gravitational moment.

The purpose of the present article is to show that a washboard pattern can develop with only one pass of a plough, so that the wake from a previous passage is not necessary. More specifically, we present experiments and a simple theoretical model to demonstrate that an object towed horizontally over a flat granular surface can leave behind a washboard. Moreover, the material composing the underlying substrate need not be granular: we find that washboards can be permanently imprinted on viscoplastic fluids or ephemerally generated on viscous fluids. Thus, we conclude that the washboard effect is a ubiquitous phenomenon that should be expected whenever an object is towed at sufficient speed along a fluid or granular surface. Indeed, our results complement a rather different experiment (Hewitt, Balmforth & McElwaine 2011) that we conducted to show that paddles pivoted above flowing water at high Reynolds number could skip continually as a result of an intrinsic instability.

We argue that the origin of all these instabilities arises from the nonlinear deformation of the granular or fluid surface: as the paddle ploughs into the material, a raised mound is pushed forward. The extent of this wedge of material controls the force exerted on the paddle, and potentially can allow the transmission of force even when the paddle lies above the undisturbed bed surface. On the other hand, the force on the paddle dictates its height, which, in turn, controls the amount of material entering the mound. The resulting coupling of the paddle and the mound generates a phase lag between the paddle's vertical position and the reaction force, capable of destabilising steady motion. The essence of this mechanism is largely independent of the material structure, thus explaining the ubiquitous nature of the instability.

2. Experiments

2.1. *The setup*

The setup of our experiment is sketched in figure 1: a trolley placed on an open-topped rectangular channel was attached to a string wound around a motorised spindle so that the trolley could be towed along the channel at fixed speed, the sides of the channel acting like the rails of a track. On the trolley a wooden ruler was pivoted, such that the ruler could rotate freely in the vertical plane aligned with the towing direction. A Plexiglas plate (the 'paddle') was attached to the end of the ruler and counterbalancing weights added to control the net downward moment, M, acting on

Ballotini	1500 kg m^{-3}	Internal friction angle ϕ : 24°
Carbopol	1000 kg m^{-3}	Yield stress τ_y: 30 ± 10 Pa
		Consistency K: 7 Pa s^n, exponent n: 0.7
Golden syrup	1470 kg m^{-3}	Viscosity μ: 15 Pa s
	1360 kg m^{-3}	Viscosity μ: 2 Pa s

TABLE 1. Properties of the experimental substrates, including a Herschel–Bulkley fit (Roberts & Barnes 2001) to the Carbopol rheology based on data from a parallel-plate rheometer.

the paddle. These counterbalancing weights contributed insignificantly to the overall moment of inertia, $\mathscr{I}$, of the pivoted ruler and paddle. The channel was filled either with 1 mm diameter glass ballotini (the granular bed) or a fluid, to a depth of 2.5 cm, and the paddle towed along this substrate surface at different speeds. The towing speed could be varied from 7 cm s^{-1} up to 53 cm s^{-1}, and the net turning moment on the paddle in its equilibrium position ranged from 0.002 to 0.06 N m. The channel was 10 cm wide, 6 cm deep and 3 m long, the paddle tip was 5 cm wide (centred in the middle of the channel), a distance $a = 23$ cm from the pivot, and made an angle of 30° with the surface of the substrate.

Table 1 summarises some properties of the materials used as a substrate. We used two different kinds of fluids: viscoplastic and viscous. The viscoplastic fluids (e.g. Bird, Dai & Yarusso 1983) were an aqueous Carbopol solution (a synthetic polymeric gel, produced by dissolving Carbopol Ultrez 21 in water to a concentration of 0.3 % by weight and adjusting its pH to ∼6 using sodium hydroxide), which possesses a significant yield stress and a shear-thinning nonlinear viscosity (Roberts & Barnes 2001), and 'joint compound' (a commercially available, kaolin-based suspension with a little extra water mixed in). Using a parallel-plate rheometer, the yield stress of the Carbopol was measured to be 30 ± 10 Pa and its rate-dependence was fitted to a Herschel–Bulkley model (table 1; cf. Roberts & Barnes 2001). The joint compound was estimated to have a similar yield stress but was difficult to characterise accurately because of its tendency to dry out. For the viscous fluids we used golden syrup with two different sugar concentrations; the corresponding viscosities are quoted in table 1. To remove any surface undulations for the granular and viscoplastic substrates, before each pass of the paddle the surface was carefully smoothed by dragging a rectangular plate with the same width as the channel along the length.

2.2. *Phenomenology*

For all the materials placed in the channel, we were able to tune the imposed moment so that the paddle did not remain steady as it was towed along the surface, but rocked up and down once the towing speed exceeded a threshold. Below the threshold, the paddle dug out a shallow, uniform furrow in the substrate, displacing a small amount of the material to either side (which, in the case of syrup, slowly levelled out as the substrate flowed back to equilibrium). Above the threshold, and when the paddle was started off at the undisturbed surface of the substrate, the paddle oscillated vertically with an amplitude that increased after a few wavelengths to a roughly steady level. If, instead, the paddle was allowed to drop abruptly onto the surface as towing began, the paddle bounced a number of times before settling into the same rhythm. Just beyond the threshold, the paddle clearly remained in contact with the substrate during the
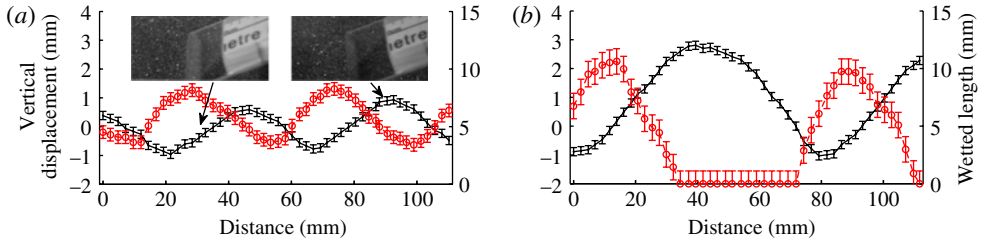
FIGURE 2. (Colour online) Height of the paddle tip above the undisturbed surface (dots, left axis), and wetted length of the paddle (circles, right axis). The error bars reflect the resolution of the video. The paddle has moment 0.005 N m and horizontal velocity: (*a*) 22 cm s^{-1}; (*b*) 36 cm s^{-1}.
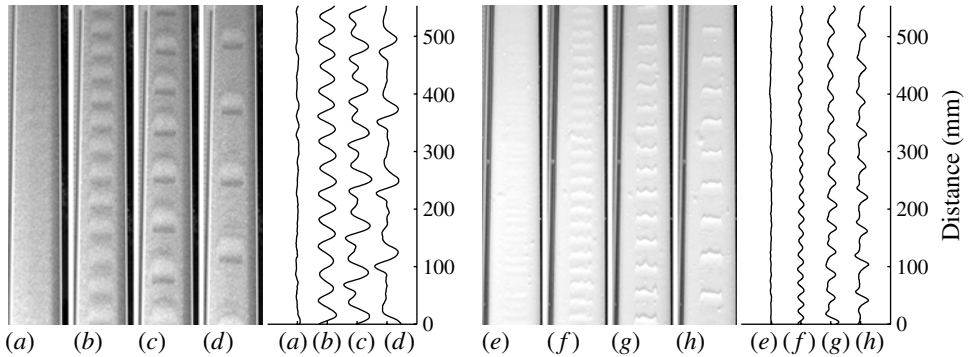

FIGURE 3. (*a–d*) Overhead photographs of the glass bead track after one pass of the paddle (from bottom to top in these images). The paddle has moment 0.005 N m and horizontal velocity (*a*) 14 cm s^{-1}, (*b*) 22 cm s^{-1}, (*c*) 36 cm s^{-1}, (*d*) 53 cm s^{-1}. On the right are average light intensity measurements derived from the centre-line of these images. (*e–h*) A similar picture for the joint compound when the paddle has moment 0.034 N m and horizontal velocity (*e*) 10 cm s^{-1}, (*f*) 22 cm s^{-1}, (*g*) 36 cm s^{-1}, (*h*) 53 cm s^{-1}.

rocking motion; once the towing speed was sufficiently in excess of the threshold, however, the paddle actually took off from the surface during part of each oscillation.

These two variants of the rocking motion are illustrated in figure 2, which shows data extracted from video footage taken with a high-speed camera (300 frames s^{-1}). The recording captures a small number of the oscillations of the paddle as it moves through the field of view, and the figure plots the vertical position of the tip of the paddle and the 'wetted length' (the length of the paddle in contact with the deforming substrate). In the example on the left, the paddle remains in contact with the substrate, whilst the paddle takes off in the other example and the wetted length vanishes over the airborne section of the trajectory.

The oscillatory rocking of the paddle carved out a washboard pattern in the substrate; photographs of sample patterns imprinted on substrates made from glass beads and the joint compound are shown in figure 3. The patterns have a distinctive shape in both the longitudinal (aligned with the towing direction) and transverse directions, reflecting the three-dimensional deformation of the substrate. Nevertheless, over the central sections of the pattern the structure was largely uniform in the

transverse direction, and visual observations suggested that the lateral deflection of the substrate was small everywhere except close to the sides of the paddle.

The elevation changes (of the order of 1 mm) in the free surface underlying the patterns in photographs like those in figure 3 are not straightforward to measure directly from the images. However, the light intensity variations provide an alternative proxy that is more accurately measured. Such intensity profiles are obtained by averaging the image brightness across the roughly two-dimensional central band of the pattern (around 2 cm wide), and then dividing by a least-squares quadratic fit to remove the background variation with the longitudinal direction; the results are seen in figure 3. The peak-to-trough variations of this proxy provide a convenient measure of the pattern's 'amplitude' for a relatively large number of undulations (compared with the number of oscillations accessible with the high-speed camera, from which we obtain amplitude measurements of the paddle tip).

2.3. *Trends*

Figure 4 provides a summary of the observed trends in measurements from experiments with varying towing speed and moment, using substrates of ballotini, Carbopol, and syrup. Figure 4(*a–c*) shows peak-to-trough amplitudes of the vertical position of the paddle tip, with the dotted segments in the lines distinguishing experiments in which the paddle was always in contact with the surface from those for which the paddle became airborne. Figure 4(*d–f*) shows the wavelengths of the imprinted patterns and the corresponding oscillation periods. The 'intensity amplitudes' of the patterns for ballotini and Carbopol are displayed in Figure 4(*g–i*). At low towing speeds, there was no obvious oscillation of the paddle tip, nor a recognisable pattern in the intensity variations (cf. figures 3*a* and 3*e*). From the video footage and photographs, we therefore estimated the noise level for each material; this level is shown by the dashed line on the figures.

For the syrup, the washboard pattern was only visible for a short time after the passage of the paddle, and the surface was relatively rough because of finer filaments of syrup drawn out from the surface as the paddle took off. This complex pattern structure made it difficult to extract reliable data for that material, and coupled with its messy adhesive nature and the need to avoid excessive evaporation from creating a superficial skin layer, this led us to perform fewer experiments for the syrup.

Overall, the ballotini experiments display a sharp threshold for the onset of the washboarding instability (figure 4*a*), that varies with the imposed moment. Once airborne, the wavelength, period and amplitude show systematic variations with both speed and moment. However, the strength of the imprinted pattern varies relatively weakly with those parameters.

By contrast, the transition to washboarding is much smoother for the viscoplastic materials (and also the syrup), and the wavelengths and periods are insensitive to the imposed moment. In fact, a residual washboard pattern appeared to form even at low speeds or high moments for these viscoplastic materials. This pattern was close to our estimates of the noise level, and is illustrated further in figure 4(*i*), which shows a series of experiments using Carbopol and covering a relatively wide range of moments with fixed towing speed. Despite the low-amplitude oscillations at the higher moments seen in this figure, there is a recognisable increase in amplitude for moments below 0.026 N m. We tentatively identify those moments as characterising the transition to washboarding and interpret the residual oscillations at larger moments as due to a different physical effect. Indeed, the low-level amplitudes and the corresponding wavelengths appear to be largely independent of the towing speed, and visual
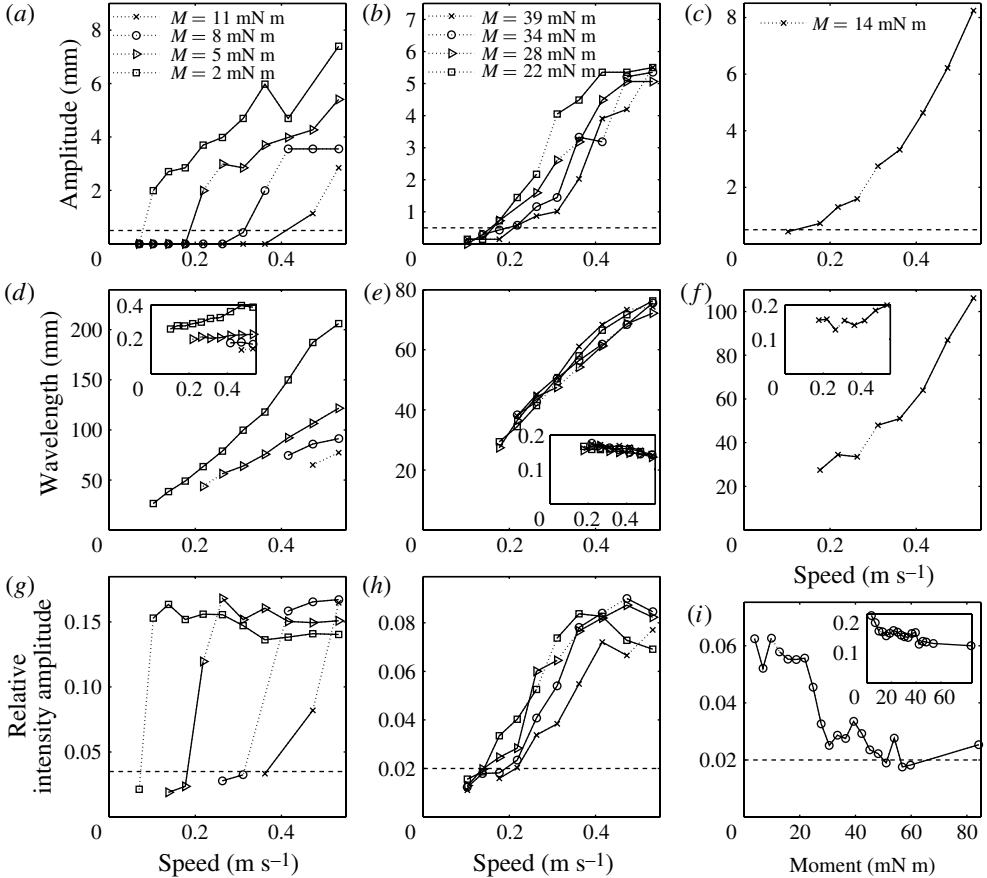
FIGURE 4. Measurements of amplitude, wavelength and period for substrates composed of ballotini (first column, *a*, *d* and *g*), Carbopol (second column, *b*, *e* and *h*, and the final panel *i*) and syrup (*c* and *f*), in suites of experiments varying the towing speed and imposed moment. The data for each moment are connected by solid lines except for the segment shown dotted, which distinguishes cases in which the paddle was always in contact with the surface (lower speeds) from experiments in which the paddle became airborne (higher speeds). The top row (*a*–*c*) shows the peak-to-trough amplitude of the oscillations in the vertical position of the paddle tip. The middle row (*d*–*f*) shows the wavelength of the imprinted pattern, with insets showing the corresponding oscillation period in seconds. The bottom row (*g*–*i*) shows the peak-to-trough amplitude of the intensity variations in overhead photographs, and the inset in (*i*) shows the corresponding periods. The dashed lines in (*a*–*c*) and (*g*–*i*) indicate our estimate for the noise level below which oscillations are unidentifiable. In (*d*–*f*), the errors are approximately ±5 mm.

observations suggested that the residual oscillations may have been driven by noise from the towing mechanism. One possible explanation for the noise-driven oscillations is viscoelastic deformation below the yield stress (damped elastic-like vibrations were visible in high-speed footage for both viscoplastic fluids), implying a connection with the troublesome phenomenon of 'roaring rails': short wavelength undulations on the the surface of rail tracks that are thought to result from a natural frequency of the elastic vibration of the rails pinned to their sleepers (Gassie, Edwards & Shepherd 2007).
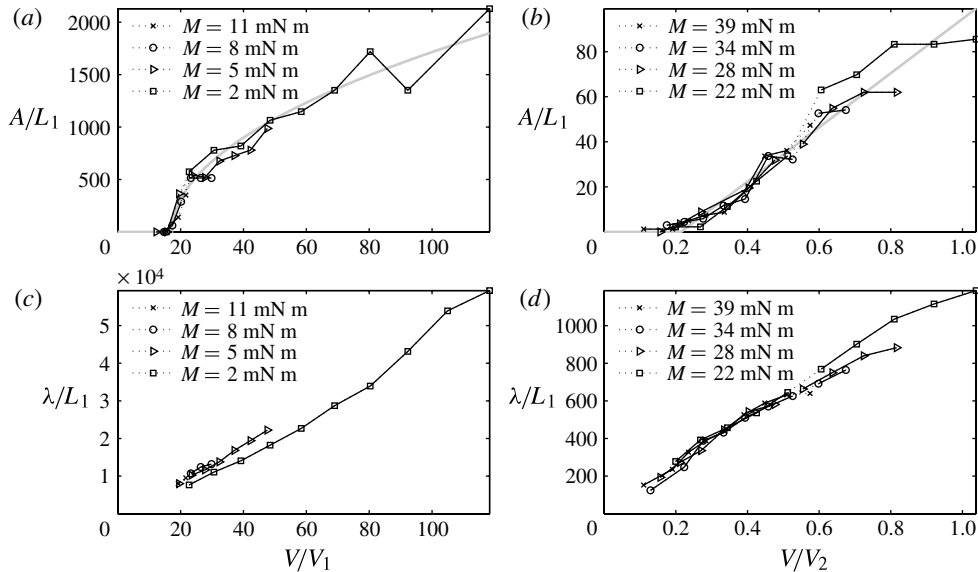
FIGURE 5. Scaled amplitude (A/L_j) and wavelength (λ/L_j) against scaled towing speed (V/V_j) for (*a,c*) ballotini ($j = 1$) and (*b,d*) Carbopol ($j = 2$), where $V_1 = M/(\mathscr{I}W\rho ga)^{1/2}$, $L_1 = (M/W\rho ga)^{1/2}$, $V_2 = M/(\mathscr{I}W\tau_y)^{1/2}$ and $L_2 = M/W\tau_y a$. The grey curve in (*a*) is a best fit of the form $A/L_1 \propto \max(0, V/V_1 - \gamma)^{1/2}$, expected beyond a Hopf bifurcation at $V = \gamma V_1$; in (*b*) the grey line shows a linear fit.

2.4. *Scaling*

To elucidate the dependence on the moment for the ballotini and Carbopol, we have attempted to non-dimensionalise the data to collapse them onto common curves. At our disposal for this task, relevant dimensional parameters governing the motion of the paddle include the towing speed, V, the moment, M, the moment of inertia, $\mathscr{I}$, the distance from the paddle tip to the pivot, a, and the paddle's width W (only the speed and moment varied significantly between experiments). For the granular bed, the only additional dimensional parameters are the density, ρ, and gravity, g. A satisfying collapse of the ballotini data is achieved by scaling the towing speed with the velocity scale $V_1 = M/(\mathscr{I}W\rho ga)^{1/2}$, and the amplitude and wavelength with the length scale $L_1 = (M/W\rho ga)^{1/2}$, as shown in figure 5. The scaled amplitude variation is suggestive of a Hopf bifurcation, varying with the square root of $V/V_1 - \gamma$, where γ is the threshold value. Note that this scaling behaviour is different from that found by Bitbol *et al.* (2009), who suggest that the threshold velocity for washboarding is proportional to $M^{1/4}$. However, their experiments studied repeated passes of a paddle or wheel, corresponding to a potentially different threshold. In addition, in their experiments weights were added directly to the towed object and were much larger than that of the supporting arm so that $\mathscr{I}g \approx aM$, reducing the number of available dimensional parameters.

For the Carbopol, we can also incorporate the yield stress, τ_y, into the scaling, focusing on the plastic behaviour rather than the rate-dependent rheology of that material. In this case, an important key to the best scaling is provided by the period data in figure 4, which is largely independent of M, signifying that the scaling of time must also be so. We find that the most suitable reduction of the data is furnished by
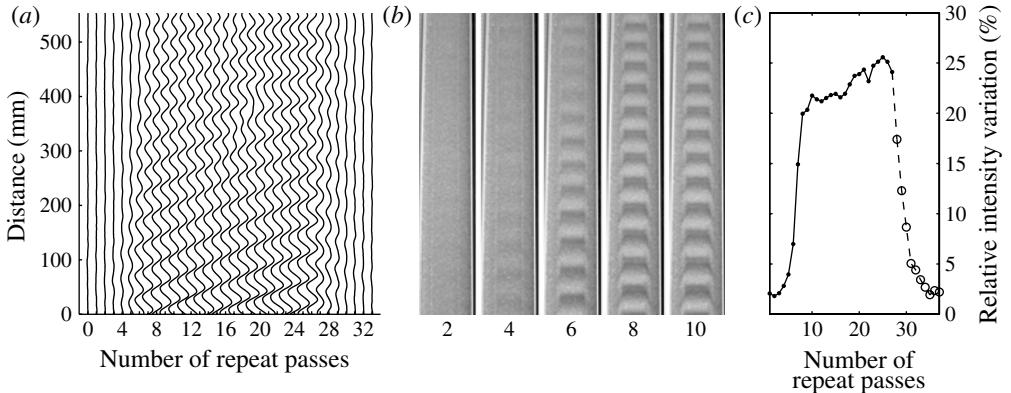
FIGURE 6. (*a*) Intensity variations in overhead photographs of the glass bead track after each repeat pass. (*b*) Examples of the photographs after 2, 4, 6, 8 and 10 passes of the paddle. (*c*) Peak-to-trough amplitude of intensity variations after each pass. The moment was 0.008 N m and horizontal velocity 22 cm s^{-1} for the first 26 passes, after which the velocity was reduced to 10 cm s^{-1} (shown by the dashed line in (*c*)) and the pattern then decays back to a flat bed.

the velocity and length scales, $V_2 = M/(\mathscr{I}W\tau_y)^{1/2}$ and $L_2 = M/W\tau_y a$; see figure 5. The same scaling is also found to work for the joint compound.

For all three materials, scaling the speed linearly with the moment collapses the thresholds for both instability and take-off. However, the scalings required to collapse the amplitude and wavelength data are quite different for the ballotini and viscoplastic fluids. A different scaling still was found for our paddle-skipping experiments on water, for which the threshold speed scales better with $M^{1/2}$ (Hewitt *et al.* 2011). Thus, although the washboarding phenomenon occurs on all the materials, the quantitative details are different in each case, which we presume to arise from the differing way in which the substrate transmits force to the paddle.

2.5. *Repeat passes*

The detection of a clear threshold for washboarding for the ballotini motivated us to explore the dynamics a little further for this material. In particular, the earlier experiments of Taberlet *et al.* (2007) led us to consider whether the onset of instability was modified when the paddle was allowed to run over its own wake. To this end, we performed a series of experiments in which the paddle was repeatedly run down the channel, without flattening the substrate surface between each pass, and towed from the same starting position (a horizontal launch pad held 3.5 cm above the ballotini). As illustrated by the sequence of photographs in figure 6, although the towing speed was set below threshold for the moment applied, after a few passes, a washboard still emerged, with its amplitude growing with each pass. After about ten passes, the growth largely stopped, leaving a pattern in which the individual undulations moved down the channel a short distance with each passage of the paddle. In fact, as seen in figure 6, the pattern moves with a well-defined positive phase displacement except around the merging of dislocations in the pattern.

Thus, the onset of washboarding certainly depends upon whether the towed device is able to run over its own wake. In this sense, we conclude that the instability described earlier is a form of absolute instability, whereas that evident in figure 6 effectively has periodic boundary conditions and is consequently convective (the boundary conditions are not quite periodic, since the paddle always starts each pass at the same fixed
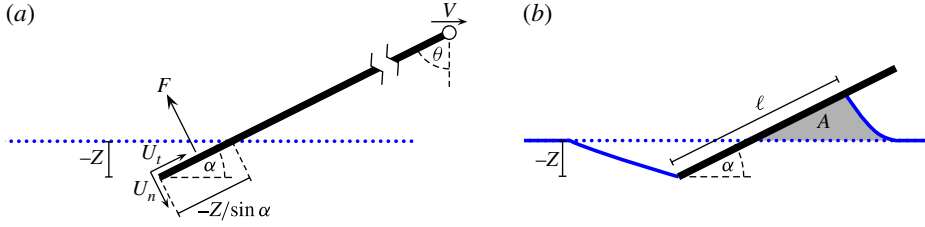
FIGURE 7. (Colour online) (*a*) In the frame of the undisturbed bed the paddle is a rigid body angled at approximately α to the horizontal, moving with velocity $(\dot{X}, \dot{Z}) \approx (V - \dot{Z}\tan\alpha, \dot{Z})$ in the horizontal and vertical directions. In coordinates normal and tangential to the paddle, the paddle's velocity is $(U_n, U_t) \approx (\dot{X}\sin\alpha - \dot{Z}\cos\alpha, \dot{X}\cos\alpha + \dot{Z}\sin\alpha) \approx (V\sin\alpha - \dot{Z}/\cos\alpha, V\cos\alpha)$. F is the normal force on the paddle. (*b*) The area A represents material displaced above the undisturbed surface, and ℓ is the wetted length.

position; there is an initial transient at the beginning of the run, observed to be a few bounces that are below the field of view in the photographs in figure 6, as the paddle adjusts to the pre-existing pattern). Furthermore, when we take the same washboard pattern after 26 passes, and then continue the repeated runs but with a slower towing speed, the paddle quickly obliterates the undulations and levels out the substrate surface (the pattern noticeably propagates backwards, rather than forwards, at this slower towing speed; see figure 6). In other words, a second threshold must exist, at a lower speed than that found for the single-pass experiments in figure 4(*a*), above which a purely convective instability appears and below which patterns do not form, even with multiple passes.

3. A simple model

The washboard dynamics observed in the experiments can be rationalised using a crude model, in which we piece together three components that describe in the broadest terms the dynamics of the paddle and substrate: (i) an equation of motion for the paddle, (ii) a mass conservation equation for the wedge of material displaced ahead, and (iii) an estimate of the lift force. Our hypothesis is that this force, F, depends on the position and velocity of the paddle, and on the size of the deformed wedge; the latter dependence is ultimately responsible for destabilising steady motion. We idealise the dynamics as two-dimensional, neglecting any flow in the transverse direction (as described earlier, this is not completely true for the experiments, although we do not believe that three-dimensional effects play a fundamental role).

3.1. *Equation of motion of the paddle*

Ignoring air resistance and friction in the hinge, the equation of motion of the paddle is

$$\mathscr{I}\ddot{\theta} = aF - M, \tag{3.1}$$

where θ is the angle of the arm (defined clockwise from vertically down; see figure 7*a*), $\mathscr{I}$ is the moment of inertia, M is the net gravitational moment, F is the normal force on the paddle from the substrate, and a is the distance from the pivot at which this force acts (approximated here by the distance from the pivot to the paddle tip).

Because the angular excursion of the paddle is small during the impact with the substrate, it is convenient to rewrite this equation of motion in terms of the Cartesian coordinates of the paddle's tip: choosing a vertical origin based on the position of the paddle when touching the undisturbed surface of the substrate, for which $\theta = \theta_0 = \pi/2 - \alpha$, and remembering that the pivot moves with prescribed horizontal velocity, denoted V, the coordinates of the paddle tip are

$$X(t) = Vt + a(\sin\theta_0 - \sin\theta) \approx Vt - a(\theta - \theta_0)\sin\alpha, \qquad (3.2)$$

$$Z(t) = a(\cos\theta_0 - \cos\theta) \approx a(\theta - \theta_0)\cos\alpha, \qquad (3.3)$$

implying

$$I\ddot{Z} = F - mg \quad \text{and} \quad \dot{X} = V - \dot{Z}\tan\alpha, \qquad (3.4)$$

where $I = \mathscr{I}/a^2\cos\alpha$ is the effective inertia of the paddle tip, and $m = M/ag$ is its effective mass. In the experiments, $\dot{Z}$ was typically much smaller than V so that $\dot{X} \approx V$.

3.2. *The wedge*

We consider the idealisation of the leading wedge shown in figure 7, with the paddle's motion broken down into components normal and tangential to the paddle, $(U_n, U_t) \approx (V\sin\alpha - \dot{Z}\sec\alpha, V\cos\alpha)$. As is clear from figure 7(a), the paddle must displace the substrate at a rate $U_n(-Z/\sin\alpha)$ per unit width. If the displaced substrate is all pushed forward into the wedge, which has area $A(t)$, then mass conservation demands that

$$\frac{\mathrm{d}A}{\mathrm{d}t} = -\frac{U_n Z}{\sin\alpha} = -(V - 2\dot{Z}/\sin 2\alpha)Z. \qquad (3.5)$$

The area, $A(t)$, can also be related to the wetted length of the paddle, ℓ, which we use below as a key quantity when estimating the lift force. More specifically, $\ell = \hat{\ell} - Z/\sin\alpha$, where $\hat{\ell}$ is the length of the wedge measured along the paddle. If we assume that the overall shape of the wedge does not change as the paddle descends into the substrate or ascends out of it, then $\hat{\ell}(t)$ is related to $A(t)$ immediately by the geometry adopted for the wedge; for greatest simplicity, we ignore the inclination of the free surface of the wedge and write $A \approx (1/2)\hat{\ell}^2\sin\alpha\cos\alpha$. Equation (3.5) can then be rewritten as

$$\tfrac{1}{2}\sin 2\alpha\,(\ell + Z/\sin\alpha)\,\dot{\ell} = -(V - \dot{Z}\tan\alpha)Z - \dot{Z}\ell\cos\alpha. \qquad (3.6)$$

3.3. *The lift force*

The normal force, F, is equal and opposite to the force acting on the substrate due to the paddle, and this force drives the substrate to flow and form the wedge. With a detailed knowledge of the fluid or granular rheology and its surface and wetting properties, the force could in principle be calculated explicitly as a function of time. This is not an easy task, however, even for the case of the Newtonian fluid, so we adopt a simpler approach by identifying a number of possible contributions to the force that we believe are most relevant, and offering dimensional estimates of their size. The basic premise of this model is that F can be expressed as a function of Z, $\dot{Z}$, and ℓ, in which case (3.4) and (3.6) combine to describe a third-order system for the paddle's elevation Z, as described below. The following expressions for $F(Z, \dot{Z}, \ell)$ are inevitably approximate, and one might also argue a case for different characterisations; in the Appendix we show how, under the restrictive assumptions of a

shallow viscous fluid layer, such an expression can be derived with a firmer grounding on the underlying fluid dynamics.

Firstly, if the paddle's speed is large, there can be an inertial force. Referring to figure 7(a), the fluid ahead of the paddle must be accelerated to move at roughly the same normal speed U_n, and the resulting rate of change of momentum gives rise to a force

$$F_i \approx C_i \rho W U_n \frac{\mathrm{d}A}{\mathrm{d}t} = -C_i \frac{\rho W U_n^2 Z}{\sin \alpha} \approx -C_i \rho W \sin \alpha \, Z \, (V - 2\dot{Z}/\sin 2\alpha)^2, \qquad (3.7)$$

where W is the paddle width and C_i is an order one dimensionless factor (cf. Clanet, Hersen & Bocquet 2004; Rosellini *et al.* 2005).

Second, an Archimedean force is generated by hydrostatic pressure within the substrate. This buoyancy force is approximately

$$F_b \approx \tfrac{1}{2} \rho g \ell^2 W \sin \alpha, \qquad (3.8)$$

given our assumptions regarding the geometry of the wedge.

Third, there are plastic internal stresses generated by the material structure of the substrate: friction for a granular material or the yield stress for a viscoplastic one. Our estimate for the corresponding forces is based on the assumption that the fluid in contact with the paddle must be moving with the same velocity, $(U_n, U_t) \approx (V \sin \alpha - \dot{Z} \sec \alpha, V \cos \alpha)$ in the normal and tangential coordinates, and that these velocities must decay to zero over a distance of order ℓ. This implies characteristic normal and total strain rates,

$$\frac{1}{\ell}(\dot{Z} \sec \alpha - V \sin \alpha) \quad \text{and} \quad \frac{1}{\ell}\sqrt{(\dot{Z} \sec \alpha - V \sin \alpha)^2 + V^2 \cos^2 \alpha}. \qquad (3.9)$$

Ignoring rate-dependent contributions, the total normal force acting on the paddle due to the plastic internal stresses can therefore be estimated to be

$$F_p \approx C_p \frac{\tau_p W \ell (V \sin \alpha - \dot{Z} \sec \alpha)}{\sqrt{(V \sin \alpha - \dot{Z} \sec \alpha)^2 + V^2 \cos^2 \alpha}}, \qquad (3.10)$$

where C_p is another dimensionless constant, τ_p is the mean plastic stress, equal to the yield stress, τ_y, for a viscoplastic material, or to the average pressure times $\tan \phi$ for the granular case, where ϕ is the internal friction angle. If the paddle digs up a largely static mound of glass beads, the pressure is roughly hydrostatic, and $\tau_p \approx (1/2)\rho g \ell \sin \alpha \tan \phi$. For relatively fast pulling speeds, with $V \gg \dot{Z}$, the contribution of granular friction is therefore much like the Archimedean force, and could be combined with F_b (cf. Percier *et al.* 2011).

Lastly there are viscous forces. Somewhat similarly, given (3.9), our estimate of these is

$$F_v \approx C_v \mu W (V \sin \alpha - \dot{Z} \sec \alpha), \qquad (3.11)$$

where μ is the dynamic viscosity, and C_v a third dimensionless constant.

In summary, taking all these different contributions to F,

$$F \approx F_b + F_p + F_v + F_i, \qquad (3.12)$$

with $F_b \propto \ell^2$, $F_p \propto \ell$, $F_v \propto V$ and $F_i \propto ZV^2$. This approximation for the force can be substituted into (3.4), which can then be solved together with (3.6) for the vertical displacement $Z(t)$ and wetted length $\ell(t)$. The paddle leaves contact with the substrate

if the wetted length decreases to zero, and in that case $F = 0$. The paddle then follows a ballistic trajectory given by $I\ddot{Z} = -mg$ until contact is resumed with the surface, when $Z = 0$.

3.4. *A viscoplastic model*

The preceding formulation applies to all the experimental substrates. To demonstrate the general behaviour, however, we now focus on the viscoplastic case and set $F = F_i + F_p + F_b$ with $\tau_p = \tau_y$, omitting the viscous contribution. We place the model system in a dimensionless form using the natural length scale $L = mg/\tau_y W C_p$ (which corresponds to the penetration depth if the weight of the paddle is supported by the yield stress of the fluid, and which is the same as L_2 used in § 2.4 but for the factor C_p) and time scale $T = L/V$. The equations can then be written in the dimensionless form

$$\mathscr{J}\ddot{Z} = -1 - \mathscr{R}\left(1 - 2\dot{Z}/\sin 2\alpha\right)^2 Z \sin\alpha + \frac{\ell \sin\alpha\,(1 - 2\dot{Z}/\sin 2\alpha)}{\sqrt{\left(1 - \dot{Z}\tan\alpha\right)^2 + \dot{Z}^2}} + \frac{1}{2}\mathscr{B}\ell^2\sin\alpha,$$

$$\frac{1}{2}\sin 2\alpha\,(\ell + Z/\sin\alpha)\,\dot{\ell} = -(1 - \dot{Z}\tan\alpha)Z - \dot{Z}\ell\cos\alpha, \qquad (3.13)$$

where

$$\mathscr{R} = \frac{\rho V^2 C_i}{\tau_y C_p}, \quad \mathscr{J} = \frac{IV^2 C_i}{\tau_y W L^2 C_p}, \quad \mathscr{B} = \frac{\rho W L^2}{m}. \qquad (3.14)$$

The dimensionless parameters $\mathscr{R}$ and $\mathscr{J}$ estimate the importance of inertia in the substrate and of the paddle; $\mathscr{B}$ measures the size of the buoyancy force. In the corresponding scaling for the granular problem, the natural choice of length scale, $L_1 = (m/\rho W)^{1/2}$, makes $\mathscr{B} = 1$ and replaces $\mathscr{J}$ and $\mathscr{R}$ by $\hat{\mathscr{J}} = IV^2/mgL_1$ and the Froude number $Fr^2 = V^2/gL_1$ (cf. Taberlet *et al.* 2007).

The system (3.13) has an equilibrium solution,

$$Z = 0, \quad \ell = \ell_0 \equiv \frac{1}{\mathscr{B}}\left(\sqrt{1 + \frac{2\mathscr{B}}{\sin\alpha}} - 1\right). \qquad (3.15)$$

Linear, normal-mode perturbations about the steady state with the form $Z \propto e^{\lambda t} = e^{(\Lambda + i\omega)t}$ satisfy a third-order ordinary differential equation with the dispersion relation

$$\mathscr{J}\lambda^3 + \ell_0\cos\alpha\,\lambda^2 + (\mathscr{R}\sin\alpha + 1 + \mathscr{B}\ell_0)\,\lambda + \frac{1 + \mathscr{B}\ell_0}{\ell_0\cos\alpha} = 0, \qquad (3.16)$$

implying the marginal stability condition

$$\mathscr{J} > \mathscr{J}_c \equiv \ell_0^2\cos^2\alpha\left(1 + \frac{\mathscr{R}\sin\alpha}{1 + \mathscr{B}\ell_0}\right). \qquad (3.17)$$

When $\mathscr{J} > \mathscr{J}_c$, the equilibrium is unstable towards oscillations. Physically, this means that the planing paddle is unstable above a threshold velocity, dependent upon the other parameters of the problem, as illustrated in figure 8. That figure also shows saturated dimensional amplitudes of the oscillatory solutions to the full nonlinear equations (3.13). For velocities just above the threshold there are periodic oscillations that do not lose contact with the surface, but at faster speeds the paddle becomes airborne (leading to the abrupt change in amplitude in figure 8*b*). Figure 9
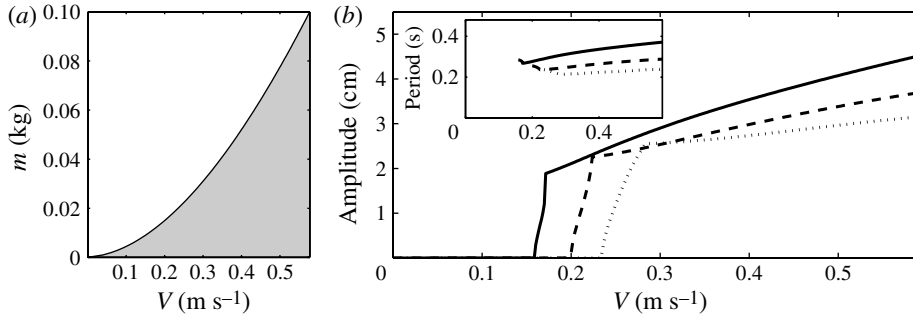
FIGURE 8. (*a*) Stability diagram for the viscoplastic model from (3.17), with $\tau_y = 30$ Pa, $\alpha = 30°$, $I = 0.03$ kg, $W = 5$ cm, $\rho = 1000$ kg m^{-3} and $C_p = C_i = 1$. The shaded region is linearly unstable. (*b*) Amplitudes of periodic solutions to the nonlinear equations (3.13) for varying velocity V at three different effective paddle masses $m = 0.01$ kg (solid), $m = 0.015$ kg (dashed), $m = 0.02$ kg (dotted). The inset shows the corresponding periods.
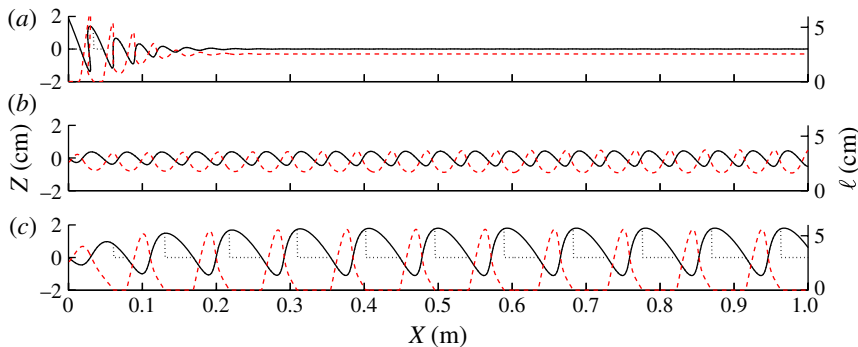

FIGURE 9. (Colour online) Some example trajectories of the viscoplastic model (3.13) (Z, solid, left axis; ℓ, dashed, right axis) plotted in terms of the dimensional variables appropriate for the experiment on Carbopol for $m = 0.01$ kg, other parameters as in figure 8, and speeds (*a*) $V = 11$ cm s^{-1}, (*b*) $V = 16.8$ cm s^{-1} and (*c*) $V = 30$ cm s^{-1}. The dotted line in (*c*) shows the imprint left on the bed (assuming no flow after the paddle detaches). Initial conditions for the first case are $\ell = 0$, $Z = 3.5$ cm, $\dot{Z} = 0$, and in the other two cases, $\ell = \ell_0$, $Z = 0$ and $\dot{Z} = -0.5V$; each of these solutions has reached a steady or regular-amplitude oscillating state by the right-hand side of the figure.

shows sample trajectories for three different velocities V, starting in each case with a perturbation about the steady planing state.

Unfortunately the stability criterion (3.17) does not suggest a straightforward scaling for the critical velocity or moment, since it depends on all three of the dimensionless parameters $\mathscr{J}$, $\mathscr{R}$ and $\mathscr{B}$. In the limit that $\mathscr{B}, \mathscr{R} \ll 1$ (that is, fluid buoyancy and inertia are negligible), the criterion reduces to $\mathscr{J} > \cot^2\alpha$, and therefore predicts that the threshold velocity scales linearly with moment, $V \propto m$. This prediction is consistent with the scaling of the experimental data for Carbopol in figure 5, even though estimates of $\mathscr{B}$ and $\mathscr{R}$ with the relevant physical parameters suggest that inertia and buoyancy are not negligible. In the same limit, from (3.16), the marginally stable mode has a dimensionless frequency of $\mathscr{J}^{-1/2}$, which corresponds to a dimensional period $\sim (I/\tau_y W)^{1/2}$ that is independent of velocity and moment, much

like the experimental observations. For larger-amplitude oscillations the period is set partly by the ballistic sections of the trajectory, which are controlled by the nonlinear dynamics of the intervening bounces, and an analytical form for the period is not available. Nevertheless, figure 8(*b*) suggests that the predicted periods remain relatively insensitive to moment and speed. Thus, not only is the natural length scale for the model, L, equivalent to that used to collapse the amplitude and wavelengths observed in the experiments, L_2, but the model also predicts the relatively weak dependence of the threshold speed and oscillation period on moment. Nevertheless, other details of the model do not match up with the experiment: the predicted amplitudes are larger and the transition to instability is much sharper.

A more detailed comparison of the model and experiment is precluded by the approximations inherent in parametrising the force. There are also a number of other factors that make direct comparison problematic: the experiments involve a certain amount of lateral flow around the paddle, which reduces the amount of substrate entering the leading wedge; the moment of inertia, though treated as constant here, varies slightly with the imposed moment; and we have ignored damping in the pivot and drag from air resistance. Finally, the substrate was always much deeper than the penetration of the imprinted pattern, and deformations appeared to be mostly localised to the surface in the high-speed video footage. However, the depth of the layer may also play a role, introducing an additional length scale (as in the lubrication theory in the Appendix).

The granular and viscous versions of the model also furnish a stable planing state at low towing speed that suffers a washboarding instability as towing becomes faster. Again, a number of dimensionless parameters control the threshold, reflecting the different forces at play, and no simple scaling of the critical towing speed with imposed moment presents itself. For the granular bed, Bitbol *et al.* (2009) suggest that the instability for convective washboarding can be characterised by the Froude number $Fr^2 = V^2/gL_1$, which measures the competition between the dynamic force and the buoyancy and frictional forces. Indeed, in our model the equivalent stability criterion to (3.17) is $\hat{\mathscr{J}} \equiv (I/m)Fr^2 > \hat{\mathscr{J}}_c$, and if the inertia were equivalent to the mass of the paddle, so $I = m$, this criterion reduces to a condition on Fr^2. In our experiments, however, m varies while I stays roughly constant, and the model is unable to explain the linear dependence of the threshold velocity on the moment suggested by figure 5.

4. Discussion

The fact that the towed paddle becomes unstable at sufficiently high speeds over all the materials in our experiments leads us to conclude that this is a fundamental instability of objects towed over deformable media. The model outlined above, although too simplistic to compare directly with the experiments, illustrates a mechanism for this generic instability, namely the build-up of the leading wedge ahead of the object. The essence of the model is that the lift force depends chiefly on the size of the wedge through some power γ of its length, $F \sim c\ell^\gamma$, where c is a proportionality factor, and the growth of that mound is dictated by the amount of material diverted into it, $\ell\dot{\ell} \sim -VZ$ (ignoring additional factors of order unity and assuming $V \gg \dot{Z}$, as is typically the case). In combination with the equation of motion of the paddle, $I\ddot{Z} = F - mg$, those approximations lead to the third-order system for the

paddle height,

$$I\,\frac{\mathrm{d}^3 Z}{\mathrm{d}t^3} + \gamma c V \ell^{\gamma-2} Z = 0, \qquad (4.1)$$

which implies that the steady planing solution ($Z = 0$ and ℓ determined by $F = mg$) is always unstable. Such a crude approximation to the dynamics is therefore not sufficient to capture the threshold for instability; the theory in § 3 represents the more elaborate version of this model, driven by the need to incorporate more of the physics so that steady planing is stable at low towing speed. Although the details depend on the particular form of the parametrised forces, the stabilising influence can be seen to stem from the vertical velocity dependence of the reaction force. This effectively introduces an additional factor $(1 - \beta \dot{Z}/V)$ to F above (β is a geometrical factor), and hence a stabilising term $\beta c l^\gamma \ddot{Z}/V$ in (4.1).

The specific form of the lift force in our model is not fundamental and alternative parametrisations can result in the same generic behaviour, as illustrated by the lubrication model in the Appendix. Indeed, we advocated essentially the same mechanism for the instability of a paddle planing over shallow water (Hewitt *et al.* 2011). In that case, the lift force arises from the dynamic pressure in the water. In the current model, our parametrisation of this particular force does not depend on ℓ, and is therefore unable to explain the instability by itself, which motivated the more detailed description of the splash dynamics in our earlier work.

The instability mechanism can be viewed in a number of complimentary ways: on one hand, the time taken for fluid to flow into the wedge and alter the wetted length ℓ introduces a destabilising lag between the paddle's height Z and the resulting restoring force. On another, the build-up of the wedge creates an asymmetry in the vertical motion of the paddle, indicating that the paddle experiences a greater force as it leaves the substrate than on its entrance, providing an extra kick. These effects are clear from the experimental measurements (figure 2), in which the oscillations of the wetted length noticeably lag behind those of the paddle, and in which the paddle ceases contact with the substrate at a higher level than that at which it makes contact. The same features are captured by the model (figure 9*c*).

The physical picture behind the instability also suggests that other details, such as the geometry of the towed object, are unlikely to be critical. Indeed, although it was clear that the geometry of the object impacted the threshold towing speed, we found that the same behaviour arose when we replaced the inclined plate with either a cylinder or a sphere (though we did not allow these objects to rotate by mounting them on an axle; rotating objects likely have different dynamics since they inhibit the formation of a wedge – see Bitbol *et al.* 2009). What is important, therefore, is simply the shape of the deformation of the substrate.

This explanation does require the substrate to be able to 'flow', however, and does not extend to rigid substrates. We did not attempt to perform experiments on a deformable solid such as an elastic layer. It is possible that the same instability resulting from nonlinear substrate deformation could occur in that case (cf. Louge & Adams 2002), but interfacial friction and the resulting stick–slip behaviour could also obscure the dynamics by prompting unsteady motion. As an aside, we also experimented with paddles pivoted by a rod rather than a ruler, allowing for sideways
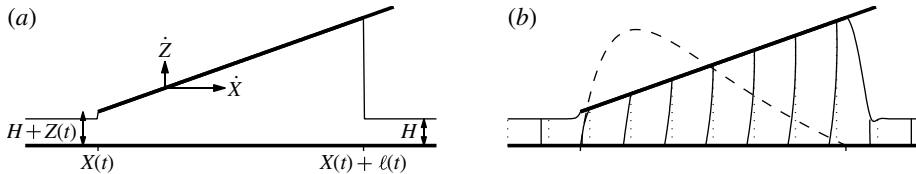
FIGURE 10. (a) Geometry of the lubrication model. (b) The inclusion of gravity and surface tension acts to smooth out the free surface ahead of and behind the paddle. The dashed line shows a typical pressure distribution and the near-vertical lines show a typical velocity profile.

tilting as well as vertical motions. In that case, the washboarding instability emerged as a fluttering mode of the paddle, suggesting an interesting interplay with the rigid body dynamics of the paddle.

Our objectives in the current study were to present exploratory experiments and a conceptual model to demonstrate how the washboarding instability occurs for a wide variety of different materials, with only a single passage of the 'vehicle', and to highlight the critical role played by surface deformation. The experiments and model could both be improved, as it is clear that many aspects of the washboarding instability remain unexplained. A more detailed exploration could expose how the threshold, oscillation amplitudes and washboard pattern depend on the splash dynamics and material behaviour, and serve as a probe into fluid and granular rheology.

Acknowledgements

Appendix. Lubrication model for a viscous fluid layer

In this appendix, we show how the normal force F can be calculated for a Newtonian viscous fluid in the context of lubrication theory. This is appropriate if the substrate is shallow and the paddle angle α is small. It is therefore not applicable to the experiments but demonstrates how, with some simplifying assumptions, the lift force can be calculated from a more detailed consideration of the fluid dynamics. For the sake of simplicity we also ignore the effects of gravity and surface tension.

The undeformed substrate occupies $0 < z < H$, and the paddle forms a rigid plate at $z = h(x, t) \equiv H + Z(t) + s(x - X(t))$, where $s = \tan \alpha$ is the slope (figure 10). We consider only the fluid flow directly beneath the paddle; the wetted length is $\ell(t)$, as in the main text, and since the paddle angle is small we may take the contact region to be $X(t) < x < X(t) + \ell(t)$. Ahead of the paddle, the fluid is a stationary uniform layer, and the wetted length (i.e. the size of the pushed forward wedge) is determined by conserving mass at the leading edge $x = X + \ell$. In reality there is a transition region where the flow adjusts to that beneath the paddle, which can be accounted for by reintroducing gravity and surface tension.

The lubrication equations are

$$u_x + w_z = 0, \quad -p_z = 0, \quad -p_x + \mu u_{zz} = 0, \quad \text{(A 1)}$$

where u and w are the horizontal and vertical fluid velocities, p is the pressure and μ is the dynamic viscosity. There is no slip at the bottom $z = 0$, so the fluid velocity there has $u = w = 0$, and the fluid velocity at $z = h(x, t)$ satisfies $u = \dot{X}$, $w = \dot{Z}$.

Integrating the momentum equations gives the standard lubrication expression

$$u(x, z, t) = \frac{z}{h}\dot{X} - \frac{z(h - z)}{2\mu}p_x, \tag{A 2}$$

and integrating the mass equation therefore gives the horizontal fluid flux

$$\frac{h}{2}\dot{X} - \frac{h^3}{12\mu}p_x = (s\dot{X} - \dot{Z})(x - X) + Q(t), \tag{A 3}$$

where the constant of integration, $Q(t)$, represents the flux at the trailing edge $x = X$. As in other lubrication problems such as slider bearings and blade coating (Quintans Carou *et al.* 2009), Q is determined by applying the condition that the pressure must be atmospheric at both ends: an integral of (A 3) gives

$$\begin{aligned} Q &= \int_X^{X+\ell} \left[(\dot{Z} - s\dot{X})(x - X) - \frac{h}{2}\dot{X}\right]\frac{\mathrm{d}x}{h^3} \bigg/ \int_X^{X+\ell} \frac{\mathrm{d}x}{h^3} \\ &= \frac{(H + Z)[\dot{Z}\ell - \dot{X}(H + Z)]}{2(H + Z) + s\ell}. \end{aligned} \tag{A 4}$$

The lift force can then be calculated from (A 3) as

$$\begin{aligned} F &= \int_X^{X+\ell} p\,\mathrm{d}x = -\int_X^{X+\ell} (x - X)p_x\,\mathrm{d}x \\ &= \frac{12\mu(\dot{X} - 2\dot{Z}/s)}{s^2}\left[\frac{1}{2}\log\left(1 + \frac{s\ell}{H + Z}\right) - \frac{s\ell}{2(H + Z) + s\ell}\right]. \end{aligned} \tag{A 5}$$

The condition of mass conservation at the leading edge is

$$\begin{aligned} (Z + s\ell)\dot{\ell} &= Q - \dot{X}Z - \dot{Z}\ell \\ &= -\frac{(H + Z + s\ell)(\dot{X}Z + \dot{Z}\ell) - \dot{X}(H + Z)H}{2(H + Z) + s\ell}. \end{aligned} \tag{A 6}$$

This is a standard Rankine–Hugoniot-style jump condition, and can be derived by balancing fluxes into and out of the moving position $x = X(t) + \ell(t)$. With the inclusion of surface tension, this shock condition is replaced by a smooth transition zone (cf. Quintans Carou *et al.* 2009 and figure 10*b*). Equation (A 6) determines the size of the leading wedge in the lubrication theory; it is slightly different from the approximation in (3.6) because the lubrication analysis allows for some back-flow, whereas (3.6) assumes that $Q = 0$.

As in the main text, a third-order system results from incorporating the expression for $F(Z, \dot{Z}, \ell)$ in (A 5) into the equation of motion $I\ddot{Z} = F - mg$, along with (A 6). There is again a steady state which is stable when the towing speed is small enough, but which becomes unstable to oscillations above a threshold speed depending upon the effective mass and inertia. Figure 11 shows the instability region and a bifurcation diagram of the amplitude of the periodic solutions analogous to that for
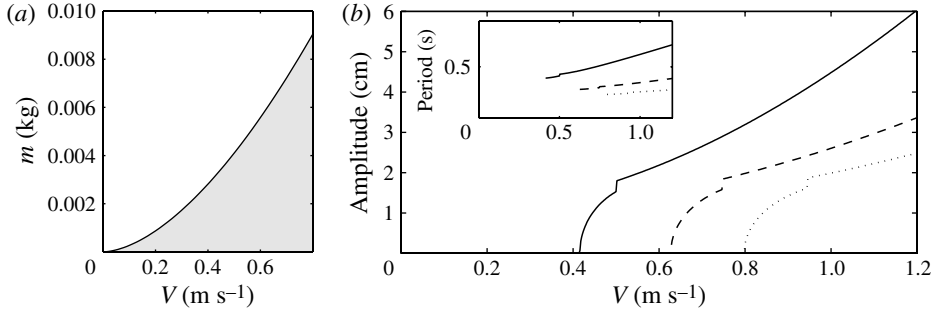
FIGURE 11. (*a*) Stability diagram for the lubrication model for varying moment and towing speed, with fluid depth $H = 1$ cm, and other parameters $\mu = 15$ Pa s, $\alpha = 30°$, $I = 0.03$ kg, $W = 5$ cm, $\rho = 1500$ kg m^{-3}. The shaded region is linearly unstable. (*b*) Amplitudes of periodic solutions to the nonlinear lubrication equations for varying velocity V at three different effective paddle masses $m = 0.003$ kg (solid), $m = 0.006$ kg (dashed), $m = 0.009$ kg (dotted). The inset shows the corresponding periods. The abrupt jump in amplitude corresponds to the periodic oscillation leaving contact with the surface.

the viscoplastic model in figure 8. The vertical jumps in the bifurcation diagram arise when the paddle first leaves contact with the fluid and becomes airborne for part of its trajectory.

REFERENCES

BIRD, R. B., DAI, G. C. & YARUSSO, B. J. 1983 The rheology and flow of viscoplastic materials. *Rev. Chem. Engng* **1**, 1.

BITBOL, A., TABERLET, N., MORRIS, S. W. & MCELWAINE, J. N. 2009 Scaling and dynamics of washboard roads. *Phys. Rev.* E **79**, 061308.

BOTH, J. A., HONG, D. C. & KURTZE, D. A. 2001 Corrugation of roads. *Physica* A **301**, 545–559.

CLANET, C., HERSEN, F. & BOCQUET, L. 2004 Secrets of successful stone-skipping. *Nature* **427**, 29.

GASSIE, S., EDWARDS, J. & SHEPHERD, J. 2007 Roaring rails, an enigma largely explained. *Intl Rail. J.* **47**, 31–33.

HEWITT, I. J., BALMFORTH, N. J. & MCELWAINE, J. N. 2011 Continual skipping on water. *J. Fluid Mech.* **669**, 328–353.

LOUGE, M. Y. & ADAMS, M. E. 2002 Anomalous behaviour of normal kinematic restitution in the oblique impacts of a hard sphere on an elastoplastic plate. *Phys. Rev.* E **65**, 021303.

MATHER, K. B. 1963 Why do roads corrugate? *Sci. Am.* **208**, 128–136.

MAYS, D. C. & FAYBISHENKO, B. A. 2000 Washboards in unpaved highways as a complex dynamical system. *Complexity* **5**, 51–60.

PERCIER, B., MANNEVILLE, S., MCELWAINE, J. N., MORRIS, S. & TABERLET, N. 2011 Lift and drag forces on an inclined plow moving over a granular surface. *Phys. Rev.* E **84**, 051302.

QUINTANS CAROU, J., WILSON, S. K., MOTTRAM, N. J. & DUFFY, B. R. 2009 Asymptotic and numerical analysis of a simple model for blade coating. *J. Engng Math.* **63**, 155–176.

ROBERTS, G. P. & BARNES, H. A. 2001 New measurements of the flow-curves for Carbopol dispersions without slip artefacts. *Rheol. Acta* **40**, 499–503.

ROSELLINI, L., HERSEN, F., CLANET, C. & BOCQUET, L. 2005 Skipping stones. *J. Fluid Mech.* **543**, 137–146.

TABERLET, N., MORRIS, S. W. & MCELWAINE, J. N. 2007 Washboard road: the dynamics of granular ripples formed by rolling wheels. *Phys. Rev. Lett.* **99**, 068003.